An Optimization Method for Quantitative Impedance Tomography

Emilie Franceschini, Serge Mensah, Loïc Le Marrec, and Philippe Lasaygues

***Abstract*—A near-field ultrasonic tomography method providing high resolution imaging for soft tissue in the reflection mode is reported. When the Born approximation is valid, the main limitation of this method is that it requires an incident pulse with infinite bandwidth, whereas the incident pulses used in practice have a limited bandwidth, which makes quantitative reconstruction impossible. The reconstructed image is qualitative in the sense that it is a band-pass filtered reconstruction of the impedance distribution. An optimization method based on the use of the geometrical information provided by the tomographic reconstruction is developed to obtain the quantitative information required. The object was approximated locally by an equivalent canonical body, on the basis of the previous global estimation. The inversion procedure is then carried out using the minimization of a cost function, which is the average over frequency of the difference between the measured field scattered by the object and the estimated field scattered by the equivalent canonical body. Assuming the object to be homogeneous by regions, the last step consists of assigning the estimated local impedance value to the region of interest. When the geometry of the real body is almost canonical, the optimization method yields accurate impedance assessments.**

I. Introduction

During the past four decades, many clinical studies have suggested that a diagnostic imaging device sensitive to differences in the tissue properties would be a useful means of improving detection and characterization procedures [1]–[4]. With this aim in view, several research workers took an early interest in quantitative reconstruction procedures and attempted to develop inverse scattering methods such as ultrasound computed tomography and, in particular, diffraction tomography methods. These methods require a plane wave incident illumination and single or multiple frequency scattering measurements at multiple transducer locations. They make it possible to reconstruct tissue parameters such as the attenuation and index of refraction [5], [6], the density and compressibility [7]–[9], or the impedance and sound speed [10]–[12]. However, most present-day ultrasound scanners are circular antenna systems working in the near field [13]–[19]. Two main approaches have been used to write the forward problem in the near field. One approach consists of using the transducer array to produce a synthetic plane wave and basing the forward problem on a plane wave assumption [13], [18], [19]. The other approach consists of taking a spherical wave incident illumination in order to formulate the forward scattering problem [20], [21]. The main advantage of the latter approach is that it takes the spatiotemporal development of the insonifying wave (in the near field) into account in order to provide better Fourier space coverage.

A forward problem modelling study using an acoustical model characterized in terms of impedance and sound speed fluctuations was recently published [22], [23]. In that paper, the medium to be imaged was insonified by a spherical wave with an infinite bandwidth, and the scattered field was measured within a circular antenna located in the near field. The forward problem formulation obtained was similar to that obtained in the far-field domain with plane wave incident illumination [12]. With both approaches [12], [22], [23], the spectral response of the medium is determined in terms of the Laplacian of the impedance and sound speed fluctuations, which give opposite local directivity diagrams: the impedance predominates in the reflection mode, and the sound speed predominates in the transmission mode. The main limitation of this impedance tomography method is that it requires an incident pulse with an infinite bandwidth, whereas the incident pulses used in practice have a limited bandwidth, which makes quantitative reconstruction impossible. The reconstructed image is qualitative in the sense that it is a band-pass filtered reconstruction of the parameter distribution [24], and the only useful information it yields is the geometrical nature and the relative amplitude echo.

The aim of the present study was to obtain quantitative information on the basis of a high resolution qualitative tomographic reconstruction [22], [23]. The optimization method used for this purpose was based on the minimization of a cost function, which quantifies the discrepancy between the measured and estimated scattered fields [25]. The search for the minimum was carried out using an iterative process consisting of resolving the forward problem at each iteration. To enhance the speed of the computations during the minimization procedure, we used an analytical formulation for the field based on a canonical approximation of the object geometry. The forward solver was therefore explicitly calculated without requiring any approximation about the fields. This method is therefore suitable for obtaining quantitative information when the

Manuscript received April 23, 2006; accepted October 17, 2006. This work was supported by Ville de Marseille, Region Provence-Alpes-Côte d'Azur, CNRS-LMA, and Eurosonic SA.

E. Franceschini, S. Mensah, and P. Lasaygues are with CNRS - Laboratoire de Mécanique et d'Acoustique, 13402 Marseille, Cedex 20, France (e-mail: franceschini@lma.cnrs-mrs.fr).

L. Le Marrec is with Laboratoire Central des Ponts et Chaussées, LCPC-BP4129, 44341 Bouguenais, France.

Digital Object Identifier 10.1109/TUFFC.2007.428

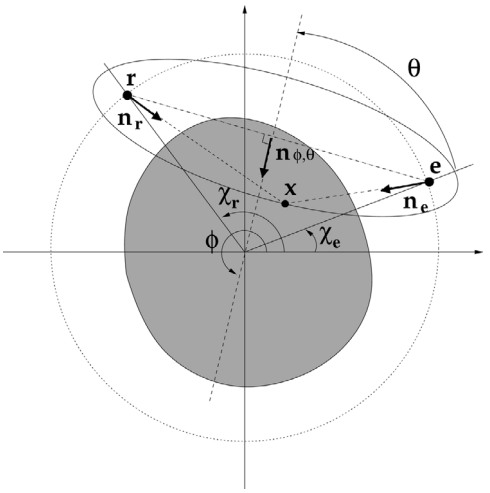

Fig. 1. Scattering acquisition configuration. In active ultrasonic tomography, a transducer **e** (which is smaller than half a wavelength) transmits a spherical wave which is scattered and recorded by a receiver **r** placed on the same spherical surface closely surrounding the organ (i.e., the breast).

geometry of the real body is almost canonical. Numerical simulations performed on a soft tissue simple phantom show how useful these optimization techniques can be when applied to tomographic applications.

II. Background: Near-Field Ultrasound Tomography

A. Definition of the Elliptical Fourier Transforms

Let us define the compact domain $\mathcal{D}$ of $\mathbb{R}^N$ $N = 2, 3$, corresponding to the organ to be imaged and the acquisition sphere (or circle, in the two-dimensional (2-D) case) $\mathcal{S}$ surrounding the compact domain $\mathcal{D}$. The acquisition sphere radius $\mathcal{R}$ is such that $\forall x \in \mathcal{D}$, $\|x\| < \mathcal{R}$. A transducer located in **e**, $\mathbf{e} \in \mathcal{S}$, transmits a spherical wave with an angular frequency ω. The field scattered by the medium is recorded in **r**, $\mathbf{r} \in \mathcal{S}$.

We take $\mathbf{n}_{\phi,\theta}$ to denote the unit vector of the mediatrix in the incident direction specified by the angles (Fig. 1):

$$\phi = \pi + \frac{1}{2}(\chi_{\mathbf{e}} + \chi_{\mathbf{r}}) \text{ the incident angle,}$$
$$\theta = \frac{1}{2}|\chi_{\mathbf{e}} - \chi_{\mathbf{r}}| \text{ the configuration angle in the plane } (\mathbf{e}, \mathbf{r}).$$

The elliptical wave vector $\mathbf{K} = k\mathbf{n}_{\phi\theta}$ is then defined. The elliptical scalar product defined for a fixed configuration (**e**, **r**) or equivalently (ϕ, θ) is introduced:

$$\begin{aligned}\mathbf{K} \otimes \mathbf{x} &= -k\,\mathbf{n}_{\phi,\theta} \otimes \mathbf{x} \\ &\triangleq -k(\|\mathbf{x} - \mathbf{e_K}\| + \|\mathbf{x} - \mathbf{r_K}\|),\end{aligned} \tag{1}$$

where $k = \omega/c_0$ is the wavenumber of the illuminating wave having sound speed c_0 in the host medium. We observe that $\mathbf{K} \otimes \mathbf{x} = \Psi$, $\Psi \in \mathbb{R}$, is the equation of the ellipsoid of focii, the transmitter and the receiver; the sum of distances from the focii is Ψ.

Let $f(\mathbf{x})$ be a well-behaved function defined over $\mathcal{D}$ and null elsewhere. The Elliptical Fourier transform $\mathcal{F}_{\mathcal{E}}$ is defined by

$$\mathcal{F}_{\mathcal{E}}(f(\mathbf{x})) = \breve{f}(\mathbf{K}) = \int f(\mathbf{x}) \frac{e^{-i\mathbf{K}\otimes\mathbf{x}}}{[\mathbf{x}]_{\mathbf{K}}}\, d\mathbf{x}, \tag{2}$$

where the distance $[\mathbf{x}]_{\mathbf{K}}$ is defined by $[\mathbf{x}]_{\mathbf{K}} = 16\ \pi^2 \|\mathbf{x} - \mathbf{e_K}\| \cdot \|\mathbf{x} - \mathbf{r_K}\|$. The inverse Elliptical Fourier transform is then defined as follows:

$$\mathcal{F}_{\mathcal{E}}{}^{-1}\left(\breve{f}(\mathbf{K})\right) = f(\mathbf{x}) = \frac{1}{(2\pi)^N} \int \breve{f}(\mathbf{K})[\mathbf{x}]_{\mathbf{K}} e^{i\mathbf{K}\otimes\mathbf{x}}\, d\mathbf{K}. \tag{3}$$

B. Forward and Inverse Tomographic Problem

We neglect the absorption-dispersion phenomena in order to concentrate on the diffusion resulting from the inhomogeneities (for practical applications of these results, a time gain compensation, TGC, should probably be used). We describe the inhomogeneous media in terms of their density ρ and velocity c distributions. Let ρ_0, c_0 be the acoustic characteristics of the surrounding medium. We introduce the parameters $2\alpha = (c^2 - c_0^2)/c^2$ and $\xi = \mathrm{Log}(z/z_0)$, corresponding to the quadratic fluctuations of velocity c and to the logarithmic variations of impedance $z = \rho c$, respectively. In view of the fact that the biological tissues are weakly inhomogeneous media ($\alpha \sim \xi \sim 10^{-2}$), we obtain, at order one in α, the following impedance-velocity propagation equation of the pressure P [12]:

$$-\frac{1}{c_0^2}\frac{\partial^2 P}{\partial t^2} + \Delta P = -\frac{2\alpha}{c_0^2}\frac{\partial^2 P}{\partial t^2} - \nabla\alpha \cdot \nabla P + \nabla\xi \cdot \nabla P. \tag{4}$$

The medium is excited with a spherical wave having angular frequency ω, the emitter being located in **e**:

$$p_i(\mathbf{x}, \mathbf{e}, \omega) = \frac{e^{ik\|\mathbf{x}-\mathbf{e}\|}}{4\pi\|\mathbf{x} - \mathbf{e}\|}. \tag{5}$$

The solution of (4) is $P = p\, e^{-i\omega t}$; p is the solution of the Helmholtz equation which can be written in its integral form:

$$\begin{aligned}p(\mathbf{r}, \mathbf{e}, \omega) = p_i(\mathbf{r}, \mathbf{e}, \omega) + \int_{\mathcal{D}} g(\mathbf{r}, \mathbf{x}, \omega)[2k^2\alpha(\mathbf{x})p(\mathbf{x}, \mathbf{e}, \omega) \\ - \nabla\alpha(\mathbf{x}) \cdot \nabla p(\mathbf{x}, \mathbf{e}, \omega) + \nabla\xi(\mathbf{x}) \cdot \nabla p(\mathbf{x}, \mathbf{e}, \omega)]d\mathbf{x},\end{aligned} \tag{6}$$

where the integration volume $\mathcal{D}$ corresponds to the compact support of α and ξ, and g is the free-space Green function; the scattered field is measured in **r**:

$$g(\mathbf{r}, \mathbf{x}, \omega) = -\frac{e^{ik\|\mathbf{r}-\mathbf{x}\|}}{4\pi\|\mathbf{r} - \mathbf{x}\|}. \tag{7}$$

We assume that the scattering is sufficiently weak to be able to linearize the inverse problem (using the Born approximation); the scattered field p_d becomes

$$p_d(\mathbf{r},\mathbf{e},\omega) = \int g\{2k^2\alpha\, p_i - \nabla\alpha\nabla p_i + \nabla\xi\nabla p_i\}\, d\mathbf{x}. \tag{8}$$

We differentiate p_i:

$$\nabla p_i(\mathbf{x},\mathbf{e},\omega) = \left(ik - \frac{1}{\|\mathbf{x}-\mathbf{e}\|}\right)\cdot\nabla(\|\mathbf{x}-\mathbf{e}\|)\cdot\frac{e^{ik\|\mathbf{x}-\mathbf{e}\|}}{4\pi\|\mathbf{x}-\mathbf{e}\|}. \tag{9}$$

In (9), $1/\|\mathbf{x}-\mathbf{e}\|$ is negligible in comparison with ik. Indeed, in soft tissues, $c_0 \approx 1540$ ms^{-1}; and in the near field zone of interest, $\|\mathbf{x}-\mathbf{e}\| \approx 10^{-2}$ m. The angular frequency components of the transmitted pulse (based on current echographs) are generally larger than $\omega_{ref} = 2\pi\cdot 2.5\ 10^6$ rad.s^{-1}; thus $k\|\mathbf{x}-\mathbf{e}\| \approx 10^2$ rad. The observation distance is greater than the wavelength.

We define $\mathbf{n}_e$ (respectively, $\mathbf{n}_r$), the unit vector along the emitter (respectively, receiver)-voxel line that we call the $\mathbf{e}-\mathbf{x}$ axis (respectively, the $\mathbf{x}-\mathbf{r}$ axis): $\mathbf{n}_e = \nabla(\|\mathbf{x}-\mathbf{e}\|)$. The scattered field is

$$p_d = -\int_{\mathcal{D}} \frac{e^{-i\mathbf{K}\otimes\mathbf{x}}}{[\mathbf{x}]_{\mathbf{K}}}\{2k^2\alpha - ik\,\mathbf{n}_e\,[\nabla\alpha - \nabla\xi]\}\, d\mathbf{x}, \tag{10}$$

and according to the definition of the elliptical Fourier transform, p_d then reduces to

$$p_d(\mathbf{K}) = -\mathcal{F}_{\mathcal{E}}\{2k^2\alpha - ik\,\mathbf{n}_e\,[\nabla\alpha - \nabla\xi]\}(\mathbf{K})_{|\mathbf{K}=k\,\mathbf{n}_{\phi,\theta}}. \tag{11}$$

The derivation rule introduced in [22], [23] yields the expression:

$$p_d(\mathbf{r},\mathbf{e},\omega) = -K^2\left[\mathcal{F}_{\mathcal{E}}(1-\mathbf{n}_e\cdot\mathbf{n}_r) * \breve{\alpha} + \mathcal{F}_{\mathcal{E}}(1+\mathbf{n}_e\cdot\mathbf{n}_r) * \breve{\xi}\right](\mathbf{K}) = -h(\mathbf{r},\mathbf{e},\omega)), \tag{12}$$

where "$*$" is the convolution product, and K is equal to $|\mathbf{K}|$; $\breve{\alpha}(\mathbf{K}) = \mathcal{F}_{\mathcal{E}}[\alpha(\mathbf{x})]$ and $\breve{\xi}(\mathbf{K}) = \mathcal{F}_{\mathcal{E}}[\xi(\mathbf{x})]$ are the elliptical Fourier transforms of the functions $\alpha(\mathbf{x})$ and $\xi(\mathbf{x})$. The term h represents the elliptical spatial transfer function of the medium in the case of a specific configuration defined by $\mathbf{e}$ and $\mathbf{r}$. This configuration involves two parameters offering opposite local directivity diagrams: the velocity predominates in the transmission mode [Fig. 2(a)], whereas the impedance predominates in the reflection mode [Fig. 2(b)]. This composite object results in a summation of the elementary contributions integrated over the whole object volume, weighted by their local directivity indexes.

When $\mathbf{n}_e = \mathbf{n}_r$, i.e., in the pure reflection mode,

$$h(\mathbf{e},\mathbf{r},\omega) = 2K^2\,\breve{\xi}(\mathbf{K})_{|\mathbf{K}=k\,\mathbf{n}_{\phi,0}} = \frac{1}{2}\mathcal{F}_{\mathcal{E}}\left[\nabla^2\xi(\mathbf{x})\right]. \tag{13}$$

When $\mathbf{n}_e = -\mathbf{n}_r$, i.e., in the pure transmission mode,

$$h(\mathbf{e},\mathbf{r},\omega) = 2K^2\,\breve{\alpha}(\mathbf{K})_{|\mathbf{K}=k\,\mathbf{n}_{\phi,\pi}} = \frac{1}{2}\mathcal{F}_{\mathcal{E}}\left[\nabla^2\alpha(\mathbf{x})\right]. \tag{14}$$

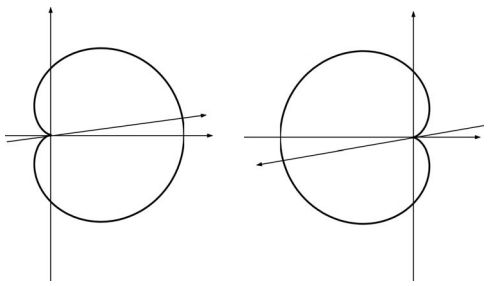

(a) (b)

Fig. 2. Directivity diagrams of α (a) and ξ (b): The velocity effects predominate in the transmission mode (a); the impedance fluctuations account mainly for the scattering in the reflection mode (b).

At this stage, we have derived a practical means of separating the respective contributions of the impedance fluctuations and those of the sound speed fluctuations to the near-field data. The application of the inverse elliptical Fourier transform enables one to reconstruct the Laplacian of one of the acoustical parameters. We choose to reconstruct the impedance and will operate in the reflection mode.

Besides, one can show that for a 2-D function f defined over $\mathcal{D}$,

$$f(\mathbf{x}) = \frac{1}{(2\pi)^2}\int_0^{\pi}\int_{-\infty}^{\infty}\mathcal{F}_{\mathcal{E}}[f](S)|S|e^{iS\mathbf{n}_\phi\otimes\mathbf{x}}[\mathbf{x}]_\phi\, dS\, d\phi = \frac{1}{(2\pi)^2}\int_{-\infty}^{\infty}\hat{p}_\phi(S)|S|e^{i\mathbf{S}_\phi\otimes\mathbf{x}}[\mathbf{x}]_\phi\, dS\, d\phi, \tag{15}$$

where $\hat{p}_\phi$ is the (standard) Fourier transform of the elliptical projection of f measured under the incidence ϕ; in a practical situation, it corresponds to the scattered field.

This formulation is the continuous expression of the classical backprojection of the filtered projection algorithm used so far in computer-assisted tomography; only the elliptical nature of the projections differs. We then obtain a solution to the inverse problem.

III. Optimization Method

The optimization method used here was based on a canonical approximation of the object geometry. Let I be the closest point to the receiver $\mathbf{r}$ located at the intersection between a specific measurement direction and the object border. We assume that the field scattered by the actual object and measured in a specific direction is fairly well approximated by the scattering resulting from a centered circular cylinder, whose radius is equal to the distance between the reference frame center 0 and the point I and which has the same acoustic properties as the object. This approximation is quite similar to the intercepting canonical body approximation (ICBA) [26]. The main idea is thus to mimic the actual body using a canonical equivalent body from which the solution of the scattering problem can be explicitly calculated and used as a forward solver during the inversion. This approximation provides,

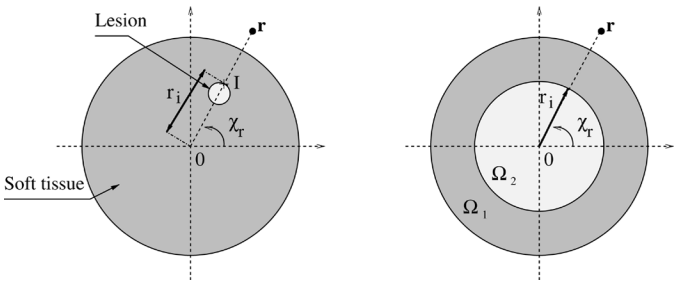

Fig. 3. Equivalent canonical configuration of the configuration studied.

therefore, fast computations and is suitable for use with iterative methods involving a large amount of data when wideband probing and several measurement angles are involved.

The object (or complex organ) studied was approximated by simple shapes representing a soft tissue with a lesion. Fig. 3 gives the canonical equivalent configuration of the configuration studied: a circular tube – medium Ω_1 – of external radius r_e (impedance z_1 and sound speed c_1), with its interior cavity – medium Ω_2 – of radius r_i (impedance z_2 and sound speed c_2). The external r_e and internal r_i radii of the equivalent tube are determined using tomographic reconstruction methods. The inverse problem is therefore reduced to the unknown parameters $\tau = (z_j, c_j)_{j=1,2}$ of the two media Ω_1 and Ω_2 and solved using the optimization method.

A. The Local Inversion Method

The inversion is carried out using scattered field measurements. The media are assumed to be linear, homogeneous, isotropic, and non-lossy. Some of the properties of the scattering problem are known: the acoustic characteristics of the surrounding medium Ω_0 (impedance z_0 and sound speed c_0), the incident field p_i located at $\mathbf{e}$, and the scattered field p_s recorded by receivers $\mathbf{r}$ at several scattering angles $\gamma = 2\theta$. The center of the acquisition circle S with radius R coincides with the center of the object.

At a single frequency, the estimated field scattered by a canonical object $p_{s,e}$ (outside the object) can be explicitly calculated using its expansion into a complete set of functions, the so-called partial waves:

$$p_{s,e}(\mathbf{r}, f) = \sum_{n=-N}^{N} b_n H_n^{(1)}(k_0 R) \exp(in\chi_{\mathbf{r}}),\ \forall \mathbf{r} \in \mathcal{S} \subset \Omega_0, \tag{16}$$

where b_n is the n-th component of the scattering coefficient exactly evaluated using the Rayleigh-Fourier method [27], [28] and $H_n^{(1)}$ is the first-kind Hankel function of order n. Convergence of this calculated quantity is obtained for $N = Ent\,(4.05(k_0 r_e)^{1/3} + k_0 r_e + 15)$ where Ent is the entire part function [29]. The unknowns τ can be determined by matching the measured field p_s with the equivalent canonical approximation model of this field $p_{s,e}$. For this purpose, we searched for the τ minimizing the single frequency cost function:

$$\mathcal{F}(\tau/\mathbf{r}, f) = \|p_s(\mathbf{r}, f) - p_{s,e}(\tau, \mathbf{r}, f)\|^2. \tag{17}$$

In order to determine the local impedance in a given observation direction, we have to solve the nonlinear equation (17) containing two unknowns (either z_1 and c_1, or z_2 and c_2 with z_1 and c_1 given). Since the impedance parameter predominates in the reflection mode (Fig. 2), if one operates in the pure reflection mode (the emitter and the receiver are merged in the backscattering), the sound speed c_j ($j = 1$ or 2) can be imposed *a priori* and the only unknown will be z_j, so that performing a single measurement at a single frequency should suffice to fully determine the local impedance value. However, the problem is less trivial, since the solution of the inverse problem is often non-unique, so that the cost function has several local minima (solutions). One way of overcoming this problem consists of adding to the cost function a regularization operator expressing some *a priori* assumptions about the solution [30], [31]. The relative confidence of the regularization procedure depends on a real positive parameter, the choice of which is rather delicate and depends on the configuration under consideration. Another solution consists of increasing the amount of data and/or using several initial guesses to find the right estimation [32], [33]. In [32], multiple frequency data are treated independently, so that several minima are obtained for each cost function. A post-processing algorithm is then applied to determine the unique solution. This procedure has the disadvantage of requiring as many minimizations as there are frequencies and it is therefore highly time consuming.

The method used here consists of using broadband ultrasonic scattering. We recently established the robustness of this method in comparison with the classical algorithm working with monochromatic signal (using ICBA as forward solver) for reconstructing the shape of non-circular tubes [33]. This method is based on the minimization of a single cost function, the mean cost function, which synthesizes all of the frequencies f_l ($l = 1 \cdots L$) included in a single measurement:

$$\begin{aligned}\overline{\mathcal{F}}(\tau/\mathbf{r}, f_l) &= \frac{1}{L}\sum_{l=1}^{L} \mathcal{F}(\tau/\mathbf{r}, f_l) \\ &= \frac{1}{L}\sum_{l=1}^{L} \|p_s(\mathbf{r}, f_l) - p_{s,e}(\tau, \mathbf{r}, f_l)\|^2.\end{aligned} \tag{18}$$

Averaging the frequencies has constructive effects on the frequency invariant minimum and destructive effects on the other minima.

B. Inversion Procedure

In what follows, we will distinguish between the unknowns we are looking for in the inverse problem and the imposed *a priori* unknowns. The *a priori* value can be either accurate or inaccurate. For each τ variable in the inverse problem, we define the exact solution $\hat{\tau}$ and the assessment domain $[\tau_m \tau_M]$.

The mean cost function depending on the variables τ_i ($i \in \mathbb{N}$)is written

$$\overline{\mathcal{F}}(\tau_i/\tau_j^a, \tau_k, \gamma), \quad i,j,k \in \mathbb{N}, \quad i \neq j \neq k,$$

when the variables τ_j^a ($j \in \mathbb{N}$, $j \neq i$) are imposed *a priori*, and the scattering angle γ and the variables τ_k ($k \in \mathbb{N}$, $k \neq i, j$) are exactly known. The solution is denoted τ_i^*. We take r_e^* and r_i^* to denote the external and internal radii of the equivalent tube, since these values are determined by the tomographic reconstruction procedure.

The inversion procedure for the optimization method involves three steps:

1. *Finding the impedance z_1 from a measurement in the pure reflection mode.* The external radius of the equivalent tube r_e^* and the sound speed imposed *a priori* c_1^a are given. During the inversion by minimization, in order to approximate a heterogeneous body (with inclusions) to a homogeneous body, we restrict the scattered field measured to the specular echo (thanks to a weighting time window). Assuming the object to be homogeneous by regions and the specular echo to be devoid of any object depth information, the estimated local value of the impedance z_1^* is allocated to the medium Ω_1.
2. *Finding the velocity c_1 from several measurements in the diffraction mode with weak scattering angles.* The values r_e^* and z_1^* are given. We operate in the diffraction mode with the first wave packet and with weakly scattered angles in order to avoid working with signals containing unwanted information about the scattering of inclusions.
3. *Finding the impedance z_2 from a measurement in the pure reflection mode.* The values r_e^*, r_i^*, z_1^*, c_1^*, and c_2^a are given. The first and second wave packets are used for the inversion procedure. The aim is to mainly use the amplitude of the second wave packet, which depends only on the impedance value z_2.

IV. Application to Simulated Data

In order to assess the validity of the reconstruction procedure presented in the previous section, we used a 2-D numerical tissue-like phantom (Fig. 4) giving a scattering response, which was computed using a finite element method (FEM). This method, which was described in [34], models the time-domain acoustic wave propagation occurring in fluid media and is based on the discretization of the mixed velocity-pressure formulation for acoustics. One of the advantages of this method is that it requires no physical approximation to be made in the framework of linear acoustics; our method thus automatically accounts for multiple scattering, refraction, and reflection. The discretization of the problem in space is based on a mixed FEM [35], and the discretization in time is performed using a 2nd-order-centered finite difference scheme. The simulation grid is surrounded by perfectly matched layers simulating unbounded domains [36].

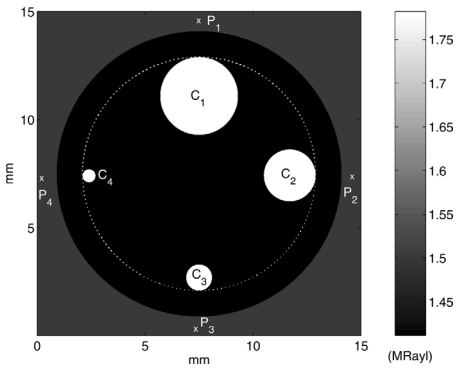

Fig. 4. Impedance map of the cylindrical academic computer phantom.

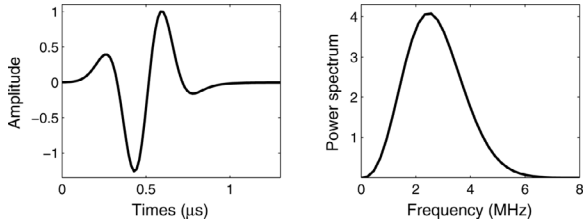

Fig. 5. A 2.5-MHz cylindrical wave used in the FEM simulations in the time and frequency domains.

The size of the spatial step in the finite element grid is taken to be one thirtieth of the wavelength. A grid consisting of 1000×1000 pixels ($\Delta x = 0.015$ mm, 1.5 cm $\times$ 1.5 cm) is used here. The ring antenna is composed of 360 equally spaced transducers (point-like transmitters and receivers, central frequency 2.5 MHz, $\lambda = 0.6$ mm) and has a radius of $R = 7.29$ mm. Each transducer transmits a short pulse, while the remaining elements act as receivers. The temporal and spectral plots of the transmitted pulses are shown in Fig. 5. The cylindrical academic phantom, which is immersed in water (density 1000 kg/m^3, velocity 1500 m/s), simulates a fluid object having the following characteristics: impedance 1.4112 MRayl and velocity 1470 m/s. The external radius of the cylinder is 6.6 mm. The radii of the holes are $r_1 = 3\lambda = 1.8$ mm, $r_2 = 2\lambda = 1.2$ mm, $r_3 = \lambda = 0.6$ mm, and $r_4 = \lambda/2 = 0.3$ mm. The inclusions have the following characteristics: impedance 1.782 MRayl and velocity 1620 m/s. We can note in Fig. 4 that each inclusion $j (j = 1 \cdots 4)$ is located in such a way that in the pure reflection mode $\mathbf{r} = \mathbf{P}_j$, the interior radius of the equivalent tube equals 5.4 mm.

Fig. 6(a) shows the impedance tomogram reconstructed with the EBP procedure when the data were acquired over a finite aperture of 10° centered on the transmitter (quasi-pure reflection mode). This reconstruction can be compared with the Laplacian of a Gaussian filter applied to the logarithmic variations of the impedance ξ map shown in Fig. 6(b). The 2-D filter used here is 20×20 pixels in size with a standard deviation of 8 pixels, and was obtained using the *fspecial('log')* command of the Matlab image pro-

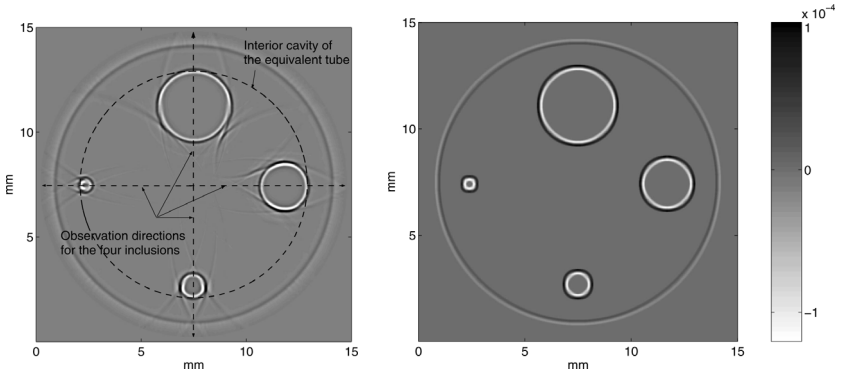

Fig. 6. (a) EBP reconstruction. (b) Laplacian of a Gaussian filter applied to the logarithmic variations of impedance ξ map.

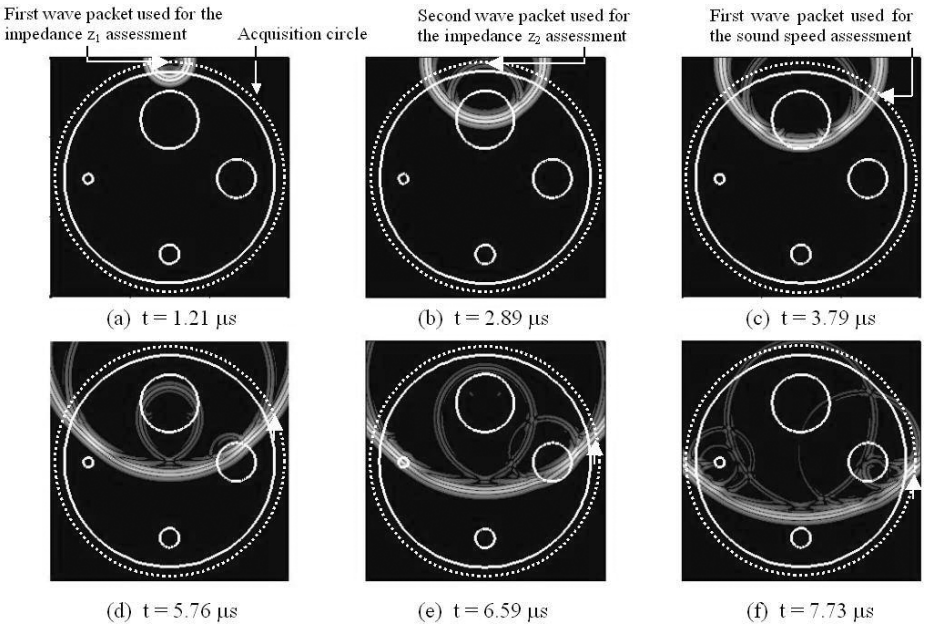

Fig. 7. Snapshots showing the propagation of a compressional wave (fluid media) through the numerical phantom when a circular wave is emitted in $\mathbf{P}_1$. The white arrows indicate the positions of the receivers used in the pure reflection or diffraction modes to assess the unknown parameters.

cessing toolbox (The MathWorks, Inc., Natick, MA). One can note the good contrast of the image and the high resolution obtained: this procedure makes it possible to detect objects of the same size as the wavelength. On the basis of the object geometry shown in Fig. 6(a), the external and internal radii of the equivalent tubes (for the observation points $\mathbf{P}_j$, $j = 1 \cdots 4$) were estimated with a relative error lower than 0.37%. Table I gives the evaluated radii. The optimization method was then applied. Fig. 7 shows the propagation of a compressional wave through the numerical phantom when a circular wave is emitted in $\mathbf{P}_1$. The white arrows show the positions of the receivers used in the pure reflection mode for the impedance assessments [Fig. 7(a) and (b)] and in the diffraction mode for the sound speed assessments [Fig. 7(c)–(f)]. This sequence of images is a useful means of checking the wave packets used in the inversion procedure.

TABLE I
INTERNAL RADIUS OF THE EQUIVALENT TUBE OBTAINED BY QUALITATIVE IMAGING (IN THE OBSERVATION DIRECTION).

	Actual radius (mm)	Evaluated radius (mm)	Relative error (%)
Matrice	6.6	6.6	0
Inclusion 1	5.4	5.42	0.37
Inclusion 2	5.4	5.41	0.19
Inclusion 3	5.4	5.4	0
Inclusion 4	5.4	5.4	0

A. Assessment of the Impedance z_1 in the Pure Reflection Mode

We consider one emitter/receiver located at $\mathbf{P}_1$ and we work only with the specular echo (Fig. 8). As shown in

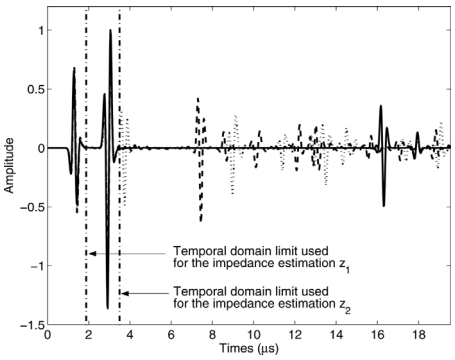

Fig. 8. Fields scattered by the equivalent tube calculated using (16) (—) and those scattered by the real object recorded at P_1 (---) and at P_4 ($\cdots$) and obtained using the finite element code (field measured in the pure reflection mode).

TABLE II
ASSESSMENT DOMAINS OF THE EQUIVALENT TUBE PARAMETERS.

τ	τ_m	$\hat{\tau}$	τ_M
z_1 (MRayl)	1.12	1.4112	1.85
c_1 (m/s)	1400	1470	1800
z_2 (MRayl)	1.12	1.782	2.58
c_2 (m/s)	1400	1620	1800

Fig. 7(a), the specular echo originates only from the wave reflected by the object matrix. Fig. 8 compares the fields backscattered by the equivalent tube calculated using (16) and by the real object (obtained with the FEM) recorded at $\mathbf{P}_1$ and $\mathbf{P}_4$. The specular echoes recorded at $\mathbf{P}_1$ and $\mathbf{P}_4$ are identical and in agreement with the specular echo given by the equivalent canonical model of the actual field. This method can therefore be expected to give an accurate assessment of the impedance z_1.

The assessment domains of the unknowns z_1 and c_1 are given in Table II. Fig. 9(a) gives the logarithm of the mean cost functions $\overline{\mathcal{F}}(z_1, c_1/r_e^*, \gamma_0)$ depending on the impedance z_1 and the sound speed c_1. The logarithm is shown here in order to enhance the lecture of the cost functions. It is worth noting that the impedance assessment z_1 is not affected by the sound speed value c_1: whatever the sound speed, the cost functions have the same appearance and have a single minimum in the assessment domain under consideration [Fig. 9(b)]. An *a priori* assumption can therefore be made about the sound speed, which is taken to be equal to that of water (soft tissue) $c_1^a = 1500$ m/s. The estimated impedance is

$$z_1^* = 1.4085 \text{ MRayl.}$$

B. Assessment of the Sound Speed c_1 in the Diffraction Mode

The medium is excited with a circular wave, with the emitter located at $\mathbf{P}_1$. The scattered field is recorded with several scattering angles in clockwise order $0° \leq \gamma \leq 180°$ (thus including the recorded points $\mathbf{P}_1 = 0°$, $\mathbf{P}_2 = 90°$, and $\mathbf{P}_3 = 180°$). Only the first wave packet in each scattered signal is used for the inversion procedure. Fig. 10 gives the mean cost functions $\overline{\mathcal{F}}(c_1/z_1^*, r_e^*, \gamma)$ depending on the sound speed c_1 for several scattering angles $\gamma = 0°$, 15°, 30°, 45°, 60°, 75°, and 90°. It can be seen here that the larger the scattering angle was, the more pronounced the minimum became, since the velocity predominates in the transmission mode. A similar analysis was carried out using the directivity diagrams of the impedance and velocity fluctuations (Fig. 2).

Fig. 11 gives the estimated sound speed (minimum of the cost function) $c_1^*(\gamma/z_1^*, r_e^*)$ with scattering angles $0° \leq \gamma \leq 180°$. With the scattering angle $\gamma \leq 8°$, the error ranged between 6 and 70 m/s: the scattering angle was too weak here to be able to estimate the velocity, since in the reflection mode, the impedance is the most robust parameter. This finding is also illustrated in Fig. 9(a) and Fig. 10 for $\gamma = 0°$: when the impedance was fixed, the cost function depending on the sound speed c_1 was quasi-null and had no distinct minimum in the pure reflection mode.

With $10° \leq \gamma \leq 84°$, the error was less than 5 m/s. At these scattering angles, the first wave packet, which originates from the matrix scattering, is clearly detached from the second wave packet, which originates from the scattering induced by the biggest inclusion [Fig. 7(c) and (d)]. Accurate velocity assessments were therefore obtained in this case.

From scattering angles greater than 85° onward, the assessment of the sound speed was found to be increasingly inaccurate, due to the multiple reflections measured at the receivers. As can be seen in Fig. 7(e), the second wave packet catches up with the first wave packet so that it is difficult to separate their time patterns. In Fig. 7(f), the scattered field measured ($\gamma = 90°$) is highly complex, since the field arising from inclusion 2 and all of the multiple reflections are measured at the same time.

We decided to estimate c_1^* by averaging the sound speeds estimated with scattering angles $25° \leq \gamma \leq 45°$. The estimated sound speed is

$$c_1^* = 1470.1 \text{ m/s.}$$

C. Assessment of the Impedance z_2 in the Pure Reflection Mode

The assessment domains of the unknowns z_2 and c_2 are given in Table II. One emitter/receiver is located at $\mathbf{P}_1$. Fig. 12(a) illustrates the logarithm of the mean cost functions $\overline{\mathcal{F}}(z_2, c_2/z_1^*, c_1^*, r_e^*, r_i^*, \gamma_0)$ depending on the impedance z_2 and the sound speed c_2. As we noted when assessing z_1, the impedance assessment z_2 is not affected by the sound speed value c_2. When a sound speed c_2 of 1500 m/s is imposed *a priori* [Fig. 12(b)], the estimated impedance for the inclusion 1 is

$$z_2^* = 1.7069 \text{ MRayl.}$$

In Fig. 13, the second wave train of the field scattered by the equivalent tube and that scattered by the real object

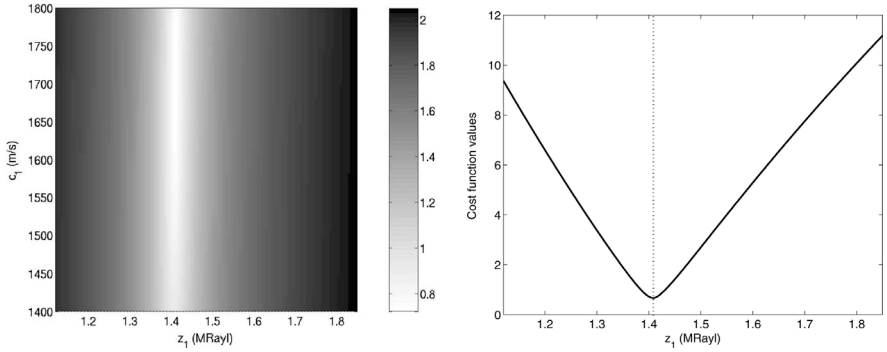

(a) (b)

Fig. 9. (a) Mean cost functions $\mathrm{Log}\left(\overline{\mathcal{F}}(z_1, c_1/r_e^*, \gamma_0)\right)$ depending on z_1 and c_1 in the pure reflection mode ($\gamma = 0°$). (b) One mean cost function $\overline{\mathcal{F}}(z_1/c_1^a, r_e^*, \gamma_0)$ depending on z_1 in the pure reflection mode when the velocity is *a priori* imposed $c_1^a = 1500$ m/s.

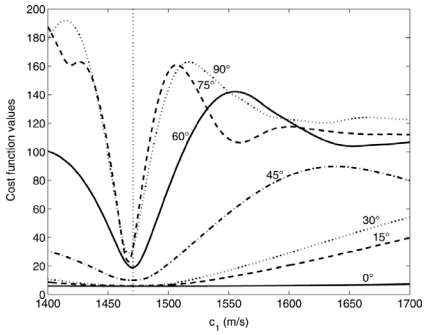

Fig. 10. Mean cost functions $\overline{\mathcal{F}}(c_1/z_1^*, r_e, \gamma_k)$ for several scattering angles k when the impedance is known ($z_1^* = 1.4085$ MRayl).

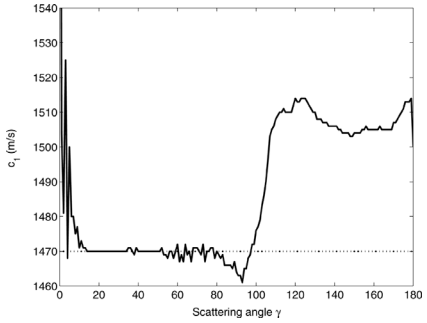

Fig. 11. Estimated velocity $c_1^*(\gamma_k/z_1^*, r_e)$ for several scattering angles $\gamma_k = 0° \cdots, 90°$ when the impedance is known ($z_1^* = 1.4085$ MRayl).

with an emitter/receiver located at $\mathbf{P}_j$ ($j = 1 \cdots 4$) (pure reflection) are compared. When the radii of the inclusions decreased, the amplitudes of the second wave trains also decreased and so did the match between the scattering induced by the equivalent interior cavity and the scattering induced by the inclusions. The estimated impedances were therefore increasingly inaccurate [Fig. 12(b)]. Table III summarizes the results.

In short, the method described here gives good results when the object under investigation can be approximated by a canonical object: the relative error in the matrix impedance assessment was found here to be 0.19%. Even when there was a large relative error in the curvature radius (66% in the case of the largest inclusion), the impedance assessment was found to be quite satisfactory (relative error 4.21%).

V. Discussion and Conclusion

As we have recalled here, it is difficult with the diffraction tomography method to obtain impedance values, but this method gives high-resolution qualitative imaging in the reflection mode. An optimization method making use of the geometrical information provided by the tomographic reconstruction was developed to obtain the quantitative information required. The object was approximated locally by an equivalent canonical body, on the basis of the previous global estimation. This canonical body is a model reduction which can be used to predict local measurements analytically. The inversion procedure was then carried out using an iterative resolution of the forward problem minimizing the difference between the measured field scattered by the object and the estimated field scattered by the equivalent canonical body. When the object geometry can be well approximated by a canonical body, using canonical body approximation as a forward solver for the inversion procedure yields accurate acoustic parameter assessments with broadband measurements. In addition, by averaging the cost function over the frequency, no additional regularization is required. Assuming the object to be homogeneous by regions, the last step in our reconstruction procedure consisted of assigning the estimated local impedance value to the region of interest.

In the present study using the simple numerical phantom, good agreement was observed between tomographic and optimization methods, in terms of the predominance of the parameters in the reflection and transmission modes. In the near field tomographic formulation, the spectral response of the medium depends on the sound speed and impedance fluctuations. The directivity diagrams for these two parameters are opposite cardiodes: the impedance predominates in the reflection mode and the sound speed in the transmission mode. The cost functions reflect this difference in terms of the sharpness of the minima. Likewise,

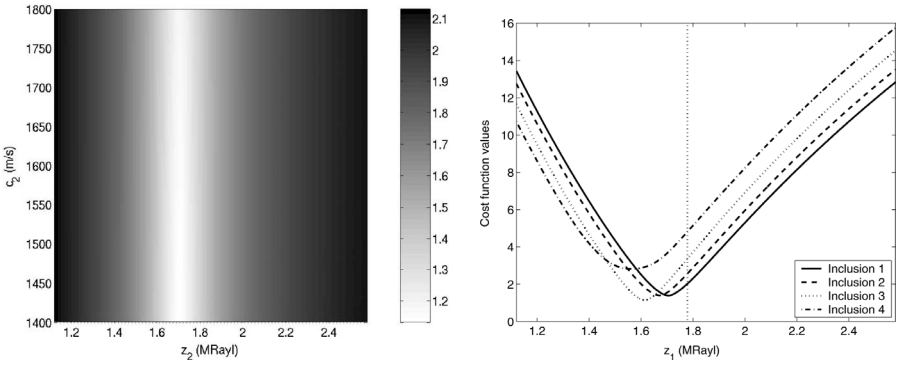

(a) (b)

Fig. 12. (a) Mean cost functions $\mathrm{Log}\left(\overline{\mathcal{F}}(z_2, c_2/z_1^*, c_1^*, r_e^*, r_1^*, \gamma_0)\right)$ depending on z_2 and c_2 in the pure reflection mode ($\gamma = 0°$). (b) For each inclusion j ($j = 1 \cdots 4$), mean cost function $\overline{\mathcal{F}}(z_2/c_2^a, z_1^*, c_1^*, r_e^*, r_j^*, \gamma_0)$ depending on z_2 in the pure reflection mode when the velocity is imposed *a priori* $c_1^a = 1500$ m/s.

TABLE III
IMPEDANCE OBTAINED BY MINIMIZATION.

	Actual impedance (MRayl)	Impedance obtained by minimization (MRayl)	Relative error on the impedance (%)	Relative error on the curvature radius (%)
Matrice	1.4112	1.4085	0.19	0
Inclusion 1	1.7820	1.7069	4.21	66
Inclusion 2	1.7820	1.6724	6.15	77
Inclusion 3	1.7820	1.6152	9.36	88
Inclusion 4	1.7820	1.5621	12.34	94

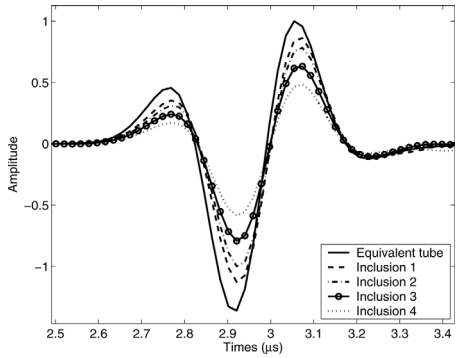

Fig. 13. Second wave trains of the fields scattered by the equivalent tube calculated using (16) (—) and by the real object recorded at P_j in the pure reflection mode.

it is worth noting the robustness shown by the impedance parameter in comparison with the sound speed parameter in the pure reflection mode when cost functions depending on these two parameters were drawn up. Moreover, since solving the forward problem based on the canonical body approximation model doesn't make any approximations about the propagation process, the optimization method yields quantitative estimations, which is not possible with the tomographic method because the transducer bandwidth is limited.

In the present study, applying optimization techniques to tomographic methods was found to be beneficial. Quite accurate local impedance assessments were obtained even when the equivalent body did not have the same curvature radius as the actual body. To approximate the holes, an equivalent object, such as a cylinder out of center with the true curvature radius, would obviously give better results. However, this would require a more sophisticated and more time-consuming forward solver such as those based on domain or volume integral representations. One could even envisage developing more complex equivalent models using finite-difference time-domain simulations [37] as forward solver in order to account for complex organ geometries such as that of the breast. As a means of solving canonical scattering problems giving exact solutions, the equivalent canonical object method is not at all time consuming and allows real-time reconstructions: a minimization involving 200 iterations (and thus 200 resolutions of the forward problem) can be carried out in this way in less than 2 minutes. Besides, the equivalent model could be further improved by developing a multilayer equivalent canonical object, accounting for elastic and lossy media, or using a three-dimensional model, for example.

ACKNOWLEDGMENTS

The authors thank the Institute for Development and Resources in Intensive Scientific computing (IDRIS), where the computations were performed. We are grate-

ful to Chrysoula Tsogka (researcher at the University of Chicago) for placing her propagation code at our disposal and to Thierry Scotti for valuable discussions.

References

[1] G. Kossoff, E. K. Fry, and J. Jellins, "Average velocity of ultrasound in the human female breast," *J. Acoust. Soc. Amer.*, vol. 53, no. 6, pp. 1730–1736, 1973.

[2] S. A. Goss, R. L. Johnston, and F. Dunn, "Comprehensive compilation of empirical ultrasonic properties of mammalian tissues," *J. Acoust. Soc. Amer.*, vol. 64, no. 2, pp. 423–457, 1978.

[3] J. Bamber and C. Hill, "Ultrasonic attenuation and propagation speed in mammalian tissues as a function of temperature," *Ultrasound Med. Biol.*, vol. 5, pp. 149–157, 1979.

[4] L. Landini, R. Sarnelli, and F. Squantini, "Frequency-dependent attenuation in breast tissue characterization," *Ultrasound Med. Biol.*, vol. 11, pp. 599–603, 1985.

[5] S. K. Kenue and J. F. Greenleaf, "Limited angle multifrequency diffraction tomography," *IEEE Trans. Sonics Ultrason.*, vol. SU-29, July pp. 213–216, 1982.

[6] J. F. Greenleaf and A. Chu, "Multifrequency diffraction tomography," in *Proc. 13th Int. Symp. Acoust. Imag.*, 1983, pp. 43–56.

[7] S. J. Norton, "Generation of separate density and compressibility images in tissue," *Ultrason. Imag.*, vol. 5, pp. 240–252, 1983.

[8] A. J. Devaney, "Variable density acoustics tomography," *J. Acoust. Soc. Amer.*, vol. 78, no. 1, pp. 120–130, 1985.

[9] S. Mensah and J.-P. Lefebvre, "Enhanced compressibility tomography," *IEEE Trans. Ultrason., Ferroelect., Freq. Contr.*, vol. 44, no. 66, pp. 1245–1252, 1997.

[10] J. P. Jones,, "Impediography, a new technique for diagnostic medicine," in *Ultrasound in Medicine*. vol. 1, D. N. White, Ed. New York: Plenum, 1975, pp. 489–497.

[11] S. J. Leeman, "Impediography equation," in *Proc. 8th Int. Symp. Acoust. Imag.*, 1978, pp. 517–526.

[12] J.-P. Lefebvre, "A linearised inverse problem: Acoustic impedance tomography in biological media," in *Electromagnetic and Acoustic Scattering: Detection and Inverse Problem*. C. Bourelli, P. Chiappetta, and B. Torresani, Eds. Singapore: World Scientific, 1988, pp. 287–301.

[13] M. P. André, H. S. Janée, P. J. Martin, G. P. Otto, B. A. Spivey, and D. A. Palmer, "High-speed data acquisition in a diffraction tomography system employing large-scale toroidal arrays," *Int. J. Imag. Syst. Technol.*, vol. 8, pp. 137–147, 1997.

[14] R. Stotzka, J. Würfel, and T. Múller, "Medical imaging by ultrasound computer tomography," in *Proc. SPIE Int. Symp. Med. Imag.*, 2002, pp. 110–119.

[15] P. Lasaygues, D. Tanne, S. Mensah, and J.-P. Lefebvre, "Circular antenna for breast ultrasonic diffraction tomography," *Ultrason. Imag.*, vol. 24, pp. 177–189, 2002.

[16] M. Ashfaq and H. Ermert, "Ultrasound spiral computed tomography for differential diagnosis of breast using conventional ultrasound system," in *Proc. 27th Int. Symp. Acoust. Imag.*, Dordrecht, The Netherlands: Kluwer Academic Publishers, 2003, pp. 627–633.

[17] J. W. Wiskin, D. T. Borup, S. A. Johnson, M. J. Berggren, and T. Abbott, "Full wave non-linear inverse scattering: High resolution quantitative breast tissue tomography," in *Proc. 28th Int. Symp. Acoust. Imag.*, 2007, pp. 183–193.

[18] A. Witten, J. Tuggle, and R. C. Waag, "A practical approach to ultrasonic imaging using diffraction tomography," *J. Acoust. Soc. Amer.*, vol. 83, no. 4, pp. 1645–1652, 1988.

[19] A. Witten, J. Tuggle, and R. C. Waag, "Ultrasonic imaging with a fixed instrument configuration," *Appl. Phys. Lett.*, vol. 53, no. 1, pp. 16–18, 1988.

[20] S. J. Norton, "Reconstruction of a two-dimensional reflecting medium over a circular domain: Exact solution," *J. Acoust. Soc. Amer.*, vol. 67, no. 4, pp. 1266–1273, 1980.

[21] S. J. Norton and M. Linzer, "Ultrasonic reflectivity imaging in three dimensions: Exact inverse scattering solutions for plane, cylindrical and circular apertures," *IEEE Trans. Biomed. Eng.*, vol. BME-28, pp. 202–220, 1982.

[22] S. Mensah, E. Franceschini, and J.-P. Lefebvre, "Mammographie ultrasonore en champ proche," *Traitement de signal, special issue Cancerology*, vol. 23, no. 3, pp. 259–275, 2006. (in French)

[23] S. Mensah and E. Franceschini, "Near-field ultrasound tomography," *J. Acoust. Soc. Amer.*, vol. 121, no. 3, pp. 1423–1433, 2007.

[24] S. Pourjavid and O. Tretiak, "Ultrasound imaging through time-domain diffraction tomography," *IEEE Trans. Ultrason., Ferroelect., Freq. Contr.*, vol. 38, no. 1, pp. 74–85, 1991.

[25] D. Colton and R. Kress, *Inverse Acoustic and Electromagnetic Scattering Theory*. 2nd ed. Berlin: Springer-Verlag, 1998.

[26] T. Scotti and A. Wirgin, "Shape reconstruction using diffracted waves and canonical solutions," *Inverse Problems*, vol. 11, pp. 1097–1111, 1995.

[27] J. J. Faran, "Sound scattering by solid cylinders and spheres," *J. Acoust. Soc. Amer.*, vol. 23, no. 4, pp. 405–418, 1951.

[28] R. D. Doolittle and H. Berall, "Sound scattering by elastic cylindrical shells," *J. Acoust. Soc. Amer.*, vol. 39, no. 2, pp. 272–275, 1966.

[29] P. W. Barber and S. C. Hill, *Light Scattering by Particles: Computational Methods*. Singapore: World Scientific Publishing Co. Pte. Ltd., 1990, pp. 30–32.

[30] A. Tikhonov, "Regularization of incorrectly posed problems," *Soviet. Math. Dokl.*, vol. 4, pp. 1624–1627, 1963.

[31] M. Y. Kokurin, "Stable iteratively regularized gradient method for nonlinear irregular equations under large noise," *Inverse Problems*, vol. 22, pp. 197–207, 2006.

[32] E. Ogam, T. Scotti, and A. Wirgin, "Non-ambiguous boundary identification of a cylindrical object by acoustic waves," *C. R. Acad. Sci. Paris*, vol. t. 329, no. Série II b, pp. 61–66, 2001.

[33] L. Le Marrec, P. Lasaygues, T. Scotti, and C. Tsogka, "Efficient shape reconstruction of non-circular tubes using broadband acoustic measurements," *Acta Acustica-Acustica*, vol. 92, no. 3, pp. 355–361, 2006, to be published.

[34] C. Tsogka, "Modélisation mathématique et numérique de la propagation des ondes elastiques tridimensionnelles dans des matériaux fissurés," Ph.D. dissertation, Université Paris Dauphine-Paris IX, Dec. 1999. (in French)

[35] E. Bécache, P. Joly, and C. Tsogka, "An analysis of new mixed finite elements for the approximation of wave propagation problems," *SIAM J. Numer. Anal.*, vol. 37, no. 4, pp. 1053–1084, 2000.

[36] F. Collino and C. Tsogka, "Application of the pml absorbing layer model to the linear elastodynamic problem in anisotropic heterogeneous media," *Geogysics*, vol. 66, pp. 294–305, 2001.

[37] C. W. Manry, J. L. Broshat, and S. L. Broshat, "FDTD simulations for ultrasound propagation in a 2-D breast model," *Ultrason. Imag.*, vol. 18, pp. 25–34, 1996.

Emilie Franceschini was born in Montpellier, France, in 1980. She received her M.S. degree in mechanical engineering from the Ecole Supérieure d'Ingénieurs de Marseille, in 2003. She is currently pursuing a Ph.D. degree at the French National Centre for Scientific Research (CNRS), Mechanics and Acoustics Laboratory, Marseille.

Her current research interests include ultrasound imaging for biomedical applications and inverse problems.

Serge Mensah was born in Metz, France, in 1961. He graduated from the Ecole Supérieure de Physique in Marseille, France, in 1984 and received his Ph.D. degree in physics in 1990.

After working for the French Navy, where he was responsible for passive sonar applications, he joined, in 1995, the Acoustics Department of the University College of Mechanics and Modeling (EGIM) in Marseille as an assistant professor. His research interests are in the fields of inverse problem and ultrasonic tomography and their applications in early cancer detection.

Loïc Le Marrec was born in Marseille, France, in 1976. He received his M.S. degree in mechanical engineering from the Ecole Supérieure d'Ingénieurs de Marseille in 2001. During his Ph.D. program at the French National Centre for Scientific Research (CNRS), Mechanics and Acoustics Laboratory, Marseille, his interest was the quantitative imaging of hard contrast objects for bone tomography. He is currently a postdoctoral fellow working on wave propagation in heterogeneous media at Laboratoire des Ponts et Chaussés-Nantes (SFGBM).

Philippe Lasaygues was born in Saint-Etienne, France, in 1965. He received a Ph.D. degree in acoustics from the University of Aix-Marseille II, Marseille, France, in 1992. He is working for the French National Centre for Scientific Research (CNRS), Laboratoire de Mécanique et Acoustique (LMA), Marseille, France, as Research Engineer. His interests include ultrasonic imaging, bio-engineering, medical and non-destructive applications, signal processing, and experimental developments. Currently, he is a member of the Société Française d'Acoustique (SFA), and of the Société Française de Génie Biologique et Médical (SFGBM).